

# Post-selected von Neumann Measurement with Superpositions of Orbital-Angular-Momentum Pointer States

Janarbek Yuanbek<sup>1,2</sup>, Yi-Fang Ren<sup>1</sup>, and Yusuf Turek<sup>1\*</sup>

<sup>1</sup>*School of Physics, Liaoning University, Shenyang, Liaoning 110036, China and*

<sup>2</sup>*School of physics and Electronic Engineering, Xinjiang Normal University, Urumqi, Xinjiang 830054, China*

(Dated: November 22, 2024)

We investigated an orbital angular momentum (OAM) pointer within the framework of von Neumann measurements and discovered its significant impact on optimizing superpositions of Gaussian and Laguerre-Gaussian (LG) states. Calculations of the quadrature squeezing, the second-order cross-correlation function, the Wigner function, and the signal-to-noise ratio (SNR) support our findings. Specifically, by carefully selecting the anomalous weak value and the coupling strength between the measured system and the pointer, we demonstrated that the initial Gaussian state transforms into a non-Gaussian state after postselection. This transition highlights the potential of OAM pointers in enhancing the performance of quantum systems by tailoring state properties for specific applications.

## I. INTRODUCTION

A Laguerre-Gaussian (LG) beam combines Laguerre polynomials with a Gaussian function and describes quantum states exhibiting spherical symmetry. The LG mode, characterized by a zero-intensity central point (ZIP), is called an optical vortex beam Nye and Berry [1]. Researchers have proposed various generation methods and experimental implementations for these beams [2–10]. In recent years, optical vortex beams have gained significant attention due to their distinctive spatial structure, which is highly useful in quantum information science [11, 12] for transmitting quantum states and generating quantum entanglement [13–15]. Allen *et al.* [16] demonstrated that the LG beam—expressed by a phase cross-section of  $\exp(il\varphi)$ , where  $l$  takes integer values—carries an orbital angular momentum (OAM) of  $l\hbar$ . Here,  $\varphi$  is the azimuthal angle, and  $l$  is the topological charge (TC). OAM beams also have numerous potential applications, including optical manipulation [17], optical communication [18–22], quantum cryptography [23, 24], quantum memory [25], chirality characterization of crystals [26], holographic ghost imaging [27], spiral phase contrast imaging [28], and particle control [29], among others. For many of these applications, state optimization processes are crucial. Quantum weak measurement techniques [30], introduced by Aharonov, Albert, and Vaidman in the late 1980s, provide a promising pathway for optimizing quantum states for specific tasks.

Researchers have confirmed the usefulness of quantum weak measurements in enhancing the inherent properties of quantum states [31–38]. Numerous theoretical and experimental studies have also explored the application of orbital-angular-momentum (OAM) pointer states [39–47]. Refs. [41, 42] introduced weak measurement methods for determining the topological charge of OAM beams and demonstrated that, for large orbital angular

momentum  $l$ , these methods are more efficient compared to earlier approaches [48–54]. One of us, in collaboration, investigated high-order Laguerre-Gaussian and Hermite-Gaussian (HG) mode pointers for postselected von Neumann measurements [40]. They have found that high-order LG and HG mode beams offer no advantage in precision measurements, as characterized by the signal-to-noise ratio (SNR), compared to the fundamental Gaussian beam. However, the superposition of high-order LG and HG modes demonstrated advantages in precision measurements due to interference effects between different modes. To our knowledge, this proposal has not yet been further explored.

In applications involving OAM pointers, optical vortex beams often undergo superposition due to imperfections in the generating apparatus and the presence of noise. However, interference can sometimes enhance the state quality and improve the resulting superposition. Therefore, it is essential to investigate the impact of postselected von Neumann-type states on the superposition of OAM beams.

In this paper, we have investigated the effects of von Neumann quantum measurements on the superposition of the LG modes with  $l = 0$  and  $l = 1$ . We perform measurements on one mode of a superposition state composed of two Laguerre-Gaussian (LG) beams, treating the spatial and polarization degrees of freedom as the measured system and pointer, respectively. The initial pointer state is a typical Gaussian state whose Wigner function consistently takes positive values. Without approximations, we determine the final state of the pointer and analyze its associated properties, including quadrature squeezing, spatial intensity distribution, second-order cross-correlation, and Wigner functions. Our findings demonstrate that, following postselected measurements, the properties of the initial pointer state undergo significant changes when appropriate coupling strength parameters and anomalous weak values of the measured system’s observables are applied. Notably, the initial Gaussian state transforms into a non-Gaussian state after the postselection process. We anticipate that the scheme presented in this study could

---

\* [yusufu1984@hotmail.com](mailto:yusufu1984@hotmail.com)

be an effective optimization method for optical vortex beams, enhancing the efficiency of various OAM-based applications.

The remainder of this paper is organized as follows. In Sec. II, we describe the setup of our theoretical model. Sec. III discusses the effects of postselected von Neumann measurements on the quadrature squeezing of superpositions of Gaussian and Laguerre-Gaussian states, demonstrating that postselected weak measurements can alter the squeezing of the initial state. In Sec. IV, we analyze the spatial distribution of the final pointer state. The influence of von Neumann measurements on the second-order cross-correlation and the phase-space distribution of the final state is explored in Sec. V. To evaluate the advantages of the initial state in precision measurements based on postselected von Neumann measurements, we study the signal-to-noise ratio (SNR) for both postselected and non-postselected cases in Sec. VI. Finally, in Sec. VII, we present our conclusions and provide an outlook on future work. Throughout this paper, we adopt the natural unit system with  $\hbar = 1$ .

## II. MODEL SETUP

The superposition of various states plays a pivotal role in quantum theory, a well-established concept with significant implications. The superposition of higher-order OAM states also finds numerous applications [55, 56]. Researchers have developed a variety of experimental techniques to generate such superpositions [55, 57–61]. Among these, a straightforward method investigated in Ref. [55] involves using a Mach-Zehnder interferometer. In this approach, the initial beam splitter divides the input beam into two paths. Each optical path passes through a hologram, creating a superposition of Gaussian and  $LG_{01}$  modes. This process is achieved by placing a hologram with a dislocation in one arm of the interferometer, as shown in Fig. 1(a). The method offers a distinct advantage: by attenuating each arm and using phase plates, one can produce arbitrary amplitude and relative phase superpositions without modifying the experimental setup. The interference pattern resulting from the superposition of the  $LG_{00}$  mode and the  $LG_{01}$  mode demonstrates this capability. We can express its mathematical expression as:

$$|\Psi_i\rangle = \frac{1}{\sqrt{1+\gamma^2}} [|\phi_0\rangle + \gamma e^{i\varphi} |\phi_1\rangle], \quad (1)$$

where  $|\phi_l\rangle = \int dx dy \phi_l(x, y) |x\rangle |y\rangle$  and the amplitude distribution of the  $LG$  modes with radial indices  $p = 0$  is characterized by

$$\phi_l(x, y) = N [x + iy \operatorname{sgn}(l)]^{|l|} \exp\left(-\frac{x^2 + y^2}{2\sigma^2}\right). \quad (2)$$

Here,  $\sigma$  represents the variance for the case state with  $l = 0$ ,  $\operatorname{sgn}(\cdot)$  is the sign function, and  $N$  is a normalizing constant ensuring that  $\int dx dy |\phi_l(x, y)|^2 = 1$ .

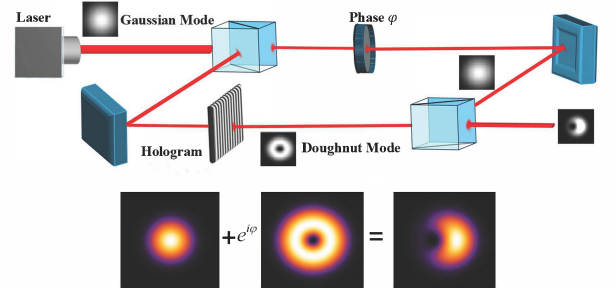


Figure 1. The setup for generating superpositions of the fundamental Gaussian mode and the  $LG_{01}$  mode, as investigated in Ref. [55]

Meanwhile, the LG mode, which can be generated from the fundamental Gaussian mode  $|0, 0\rangle$ , is expressed in the following form [62]:

$$|s, q\rangle_{LG} = \frac{1}{\sqrt{\alpha! \beta!}} (\hat{a}_+^\dagger)^\alpha (\hat{a}_-^\dagger)^\beta |0, 0\rangle_{HG}, \quad (3)$$

here,  $\hat{a}_\pm = (\hat{a} \mp i\hat{b})/\sqrt{2}$  and the integers  $\alpha$  and  $\beta$  are defined as  $\alpha = (s+q)/2$  and  $\beta = (s-q)/2$ . The parameters  $s$  and  $q$  are related to the radial and azimuthal indexes of the  $LG$  modes by the relations  $l = q$  and  $p = (s - |l|)/2$ . Furthermore,  $\hat{a}$  and  $\hat{b}$  denote the annihilation operators corresponding to the  $a$  and  $b$  modes of the  $HG$  beam. These operators act as follows:  $\hat{a}|n, m\rangle = \hat{a}|n\rangle_a |m\rangle_b = \sqrt{n}|n-1, m\rangle$  and  $\hat{b}|n, m\rangle = \hat{b}|n\rangle_a |m\rangle_b = \sqrt{m}|n, m-1\rangle$ . Using Eq. (1), we can rewrite the state  $|\Psi_i\rangle$  in terms of  $HG$  modes as:

$$\begin{aligned} |\Psi_i\rangle &= \frac{1}{\sqrt{1+\gamma^2}} \left[ |0, 0\rangle_{HG} + \frac{\gamma e^{i\varphi}}{\sqrt{2}} (|1, 0\rangle_{HG} + i|0, 1\rangle_{HG}) \right] \\ &= \frac{1}{\sqrt{1+\gamma^2}} \left[ \left( |0\rangle + \frac{\gamma e^{i\varphi}}{\sqrt{2}} |1\rangle \right) |0\rangle + i \frac{\gamma e^{i\varphi}}{\sqrt{2}} |0\rangle |1\rangle \right]. \end{aligned} \quad (4)$$

Here, the  $HG$  modes defined as

$$|n, m\rangle = \frac{1}{\sqrt{m! n!}} (\hat{a})^m (\hat{b})^n |0, 0\rangle_{HG}. \quad (5)$$

This is an entanglement state between two modes of the  $HG$  beam. In this study, we explore the properties of this state after a postselected measurement. We use the spatial and polarization degrees of freedom of  $|\Psi_i\rangle$  as the measuring system (pointer) and the measured system, respectively.

For simplicity, in this work, we consider only a measurement performed on one mode of the system. According to the standard measurement theory proposed by von Neumann [63], the coupling between the measured system and the pointer is:

$$H = g \hat{\sigma}_x \otimes \hat{P}_x. \quad (6)$$

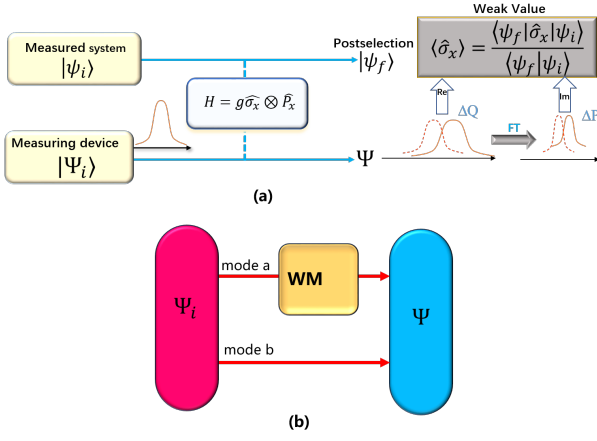


Figure 2. (a) Schematic diagram of the weak measurement (WM) process. The standard procedure of WM involves four key steps: (i) The initial state of the measured system is prepared as  $|\psi_i\rangle$ , and the measuring device is initialized in the state  $|\phi_i\rangle$ . (ii) A weak interaction occurs between the measured system and the measuring device, causing the composite system to evolve. In this model, the weak interaction is described by the Hamiltonian  $H = g \hat{\sigma}_x \otimes \hat{P}_x$ , where the coupling constant  $g$  characterizes the bilinear coupling. (iii) After some evolution, the entire system is projected onto the postselected state  $|\psi_f\rangle$  of the measured system. This postselection extracts the desired values of the system's observable by choosing a specific subensemble of samples before the final measurement. (iv) The measurement result is determined by analyzing the shifts in the pointer. In the postselected weak measurement process, the observable value expressed as a function of the weak value has its real part ( $\Re$ ) and imaginary part ( $\Im$ ) extracted from the shifts in position and momentum of the measuring device, respectively. The Fourier transform (FT) is used to convert position space into momentum space. (b) Schematic setup for preparing the state  $|\Psi\rangle$  via a postselected von Neumann measurement.

Here, the  $g$  represents the interaction coupling parameter between the pointer and the measured system, and  $\hat{\sigma}_x = |D\rangle\langle D| - |A\rangle\langle A|$  is the operator of the measured system, where  $|D\rangle = \frac{1}{\sqrt{2}}(|H\rangle + |V\rangle)$  and  $|A\rangle = \frac{1}{\sqrt{2}}(|H\rangle - |V\rangle)$  represent the diagonal and anti-diagonal polarizations in the horizontal  $|H\rangle$  and vertical  $|V\rangle$  polarization bases of the beam, respectively. The operator  $\hat{P}_x$  denotes the momentum operator of the  $a$  mode of the pointer, which is conjugate to  $\hat{X} = \int dx x|x\rangle\langle x|$ , i.e.,  $[\hat{X}, \hat{P}_x] = i$ . Assuming that the initial state of the measured system and the pointer are  $|\psi_i\rangle$  and  $|\Psi_i\rangle$ , respectively, the state  $|\psi_i\rangle \otimes |\Psi_i\rangle$  evolves under the unitary evolution operator  $\hat{U}(t) = \exp(-i \int_0^t \hat{H}_{int} d\tau)$  to:

$$\begin{aligned} |\Phi\rangle &= \exp\left(-i \int_0^t \hat{H}_{int} d\tau\right) |\psi_i\rangle \otimes |\Psi_i\rangle \\ &= \frac{1}{2} \left[ (\mathbb{I} + \hat{\sigma}_x) \otimes \hat{D}\left(\frac{\Gamma}{2}\right) + (\mathbb{I} - \hat{\sigma}_x) \otimes \hat{D}\left(-\frac{\Gamma}{2}\right) \right] \times |\psi_i\rangle \otimes |\Psi_i\rangle \end{aligned}$$

Here,  $\hat{D}(\Gamma/2) = e^{\Gamma/2(\hat{a}^\dagger - \hat{a})}$  is the displacement operator,  $\mathbb{I}$  is the  $2 \times 2$  identity matrix operator, and  $\Gamma = \frac{gt}{\sigma}$  is the coupling strength parameter. In the derivation of the above expression, we write the momentum operator  $\hat{P}$  in terms of the annihilation and creation operators,  $\hat{a}$  and  $\hat{a}^\dagger$ , as  $\hat{P} = \frac{i}{2\sigma}(\hat{a}^\dagger - \hat{a})$ , where  $\sigma$  is the size of the fundamental Gaussian beam. The parameter  $s$  is dimensionless and can take continuous values, characterizing the measurement strength. If  $0 < \Gamma \ll 1$ , the measurement is weak, whereas  $\Gamma \gg 1$ , is classified as strong. The value of  $s$  can be controlled experimentally in three ways, corresponding to adjustments in  $g$ ,  $t$ , and  $\sigma$ . Experimental research [64] has shown that the simplest and most direct way to adjust the coupling strength parameter  $s$  is by tuning the coupling duration  $t$ . Below, we assume that the change in  $\Gamma$  comes from  $t$ , while  $g$  and  $\sigma$  are fixed. For the implementation of the postselected von Neumann measurement, the postselected state  $|\psi_f\rangle$  is taken as in Eq. (7), and we can express the normalized final state of the pointer as:

$$|\Psi\rangle = \lambda \left[ (1 + \langle \hat{\sigma}_x \rangle_w) \hat{D}\left(\frac{\Gamma}{2}\right) + (1 - \langle \hat{\sigma}_x \rangle_w) \hat{D}^\dagger\left(\frac{\Gamma}{2}\right) \right] |\Psi_i\rangle, \quad (8)$$

where the normalization coefficient  $\lambda$  is defined as

$$\lambda = \left\{ \frac{1}{2} \left[ 1 + |\langle \hat{\sigma}_x \rangle_w|^2 + (1 - |\langle \hat{\sigma}_x \rangle_w|^2) \text{Re}[I_1] \right] \right\}^{-\frac{1}{2}} \quad (9)$$

with

$$I_1 = \left\{ 1 - \frac{1}{1 + \gamma^2} \left[ i\sqrt{2}\Gamma\gamma \sin(\varphi) + \frac{(\gamma\Gamma)^2}{2} \right] \right\} e^{-\frac{\Gamma^2}{2}}. \quad (10)$$

In Eq. (8), the  $\langle \hat{\sigma}_x \rangle_w$  is the weak value of the measured operator  $\hat{\sigma}_x$ . In this work, we assume the preselected and postselected states of the measured system are given by  $|\psi_i\rangle = \cos(\frac{\alpha}{2})|H\rangle + e^{i\delta} \sin(\frac{\alpha}{2})|V\rangle$  and  $|\psi_f\rangle = |H\rangle$ , respectively. For these states, the weak value  $\langle \hat{\sigma}_x \rangle_w$  is given by:

$$\langle \hat{\sigma}_x \rangle_w = \frac{\langle \psi_f | \hat{\sigma}_x | \psi_i \rangle}{\langle \psi_f | \psi_i \rangle} = e^{i\delta} \tan \frac{\alpha}{2}. \quad (11)$$

Here,  $\delta \in [0, 2\pi)$  and  $\alpha \in [0, \pi)$ . During the derivation of  $|\Psi\rangle$ , we used the mathematical definition of the displaced Fock state:

$$\hat{D}(\alpha) |n\rangle = e^{-\frac{|\alpha|^2}{2}} \sum_{k=0}^{\infty} \binom{n!}{k!}^{\frac{1}{2}} (\alpha)^{k-n} L_n^{(k-n)}(|\alpha|^2) |k\rangle, \quad (12)$$

where  $L_n^{(k-n)}(\cdot)$  are the generalized Laguerre polynomials. Equation (8) represents the final state of the pointer after the postselected von Neumann measurement. The weak value above can exceed the normal range of observable values for  $\sigma_x$  when the pre- and postselected

states are nearly orthogonal, and it can even take complex values in the case where  $\delta \neq 0$ . As mentioned in the introduction, anomalously large weak values amplify tiny system information and can also be used to optimize quantum states. Next, we examine the effects of anomalous weak values of the measured system observable on the intrinsic properties of  $|\Psi\rangle$ .

### III. EFFECTS ON QUADRATURE SQUEEZING

In this subsection, we study the effects of postselected von Neumann measurement on the quadrature squeezing of  $|\Psi\rangle$ . To discuss the squeezing phenomenon, we define the two-mode quadrature operators as [65]:

$$\hat{F}_1 = \frac{1}{2^{3/2}}(\hat{a} + \hat{b} + \hat{a}^\dagger + \hat{b}^\dagger), \quad (13)$$

$$\hat{F}_2 = \frac{1}{2^{3/2}i}(\hat{a} + \hat{b} - \hat{a}^\dagger - \hat{b}^\dagger). \quad (14)$$

One can verify that these two operators satisfies the commutation relation,  $[\hat{F}_1, \hat{F}_2] = \frac{i}{2}$ , and the corresponding uncertainty relation for their fluctuations is

$$\Delta\hat{F}_1^2\Delta\hat{F}_2^2 \geq \frac{1}{16}, \quad (15)$$

where  $\Delta F_i^2 = \langle F_i^2 \rangle - \langle F_i \rangle^2$  ( $i = 1, 2$ ). The squeezing parameter, which characterizes the quadrature squeezing of the  $i$ -th component of  $|\Psi\rangle$  (superpositions of Gaussian and Laguerre-Gaussian states), is defined as follows:

$$Q_i = \Delta\hat{F}_i^2 - \frac{1}{4}. \quad (16)$$

As we can see, the values of  $Q_i$  are bounded by  $Q_i \geq -\frac{1}{4}$ , and the  $i$ -th component of the quadrature operators of  $|\Psi\rangle$  is considered squeezed if  $-\frac{1}{4} \leq Q_i < 0$ . After some algebra, we can obtain the squeezing parameters  $Q_i$  for the final state  $|\Psi\rangle$  as:

$$\begin{aligned} Q_{1,\Phi_f} &= \frac{1}{4} \left[ \langle \hat{a}^\dagger \hat{a} \rangle + \langle \hat{b}^\dagger \hat{b} \rangle + \langle \hat{a}^\dagger \hat{b} \rangle + \langle \hat{a} \hat{b}^\dagger \rangle + \langle \hat{a} \hat{b} + \hat{a}^\dagger \hat{b}^\dagger \rangle \right] \\ &\quad + \frac{1}{8} \left[ \langle \hat{a}^2 + \hat{a}^{\dagger 2} \rangle + \langle \hat{b}^2 + \hat{b}^{\dagger 2} \rangle \right] \\ &\quad - \frac{1}{8} \left[ \langle \hat{a} + \hat{a}^\dagger \rangle + \langle \hat{b} + \hat{b}^\dagger \rangle \right]^2. \end{aligned} \quad (17)$$

$$\begin{aligned} Q_{2,\Phi_f} &= \frac{1}{4} \left[ \langle \hat{a}^\dagger \hat{a} \rangle + \langle \hat{b}^\dagger \hat{b} \rangle + \langle \hat{a}^\dagger \hat{b} \rangle + \langle \hat{a} \hat{b}^\dagger \rangle + \langle \hat{a} \hat{b} + \hat{a}^\dagger \hat{b}^\dagger \rangle \right] \\ &\quad - \frac{1}{8} \left[ \langle \hat{a}^2 + \hat{a}^{\dagger 2} \rangle + \langle \hat{b}^2 + \hat{b}^{\dagger 2} \rangle \right] \\ &\quad + \frac{1}{8} \left[ \langle \hat{a} + \hat{a}^\dagger \rangle + \langle \hat{b} + \hat{b}^\dagger \rangle \right]^2. \end{aligned} \quad (18)$$

Here,  $\langle \dots \rangle$  denotes the average values of the associated operators under the state  $|\Psi\rangle$ , and Appendix A provides the analytic expressions for these expectation values.

To clearly explain the effects of the postselected von Neumann measurement on the quadrature squeezing of  $|\Psi\rangle$ , we rely on numerical analysis and the corresponding results shown in Fig. 3. In Figs. 3(a) and (c), we plot  $Q_1$  and  $Q_2$  as functions of  $r = \sqrt{x^2 + y^2}$  for different coupling strength parameters  $\Gamma$ , while fixing the weak value parameter at  $\alpha = 8\pi/9$ . Initially, the state  $|\Psi_i\rangle$  exhibits no quadrature squeezing effect across all parameter regions. Additionally, for large anomalous weak values, such as  $\langle \sigma_x \rangle_w = 5.671$  ( $\alpha = 8\pi/9$ ), the resulting squeezing effect is greater than that of the original state ( $\Gamma = 0$ ) in the weak measurement regime. This result reflects the amplification effect of the weak value. Figs. 3(b) and (d) present the changes in  $Q_1$  and  $Q_2$  as functions of the coupling strength parameter  $\Gamma$  for different weak values while fixing  $r = 2$ . In the appropriate weak measurement regime (small  $\Gamma$ ), the squeezing of  $|\Psi\rangle$  increases with the weak value. We investigate the effects of the postselected von Neumann measurement on the properties of the output state  $|\Psi\rangle$ .

### IV. EFFECTS ON INTENSITY DISTRIBUTION

Postselected weak measurements on the measured system can alter the inherent characteristics of the pointer due to weak value amplification. This effect has also been confirmed in OAM-based pointer measurement problems. In this section, we investigate the impact of a postselected von Neumann measurement on the intensity distribution of the state, defined by superpositions of LG modes, such as in Eq. (7). We can rewrite the initial state  $|\Psi_i\rangle$  in the coordinate representation as:

$$\begin{aligned} \Psi_i(x, y) &= \langle x, y | \Psi_i \rangle \\ &= \frac{1}{\sqrt{1 + \gamma^2}} \left[ \phi_0(x, y) + \frac{\gamma e^{i\varphi}}{\sqrt{2}} \frac{1}{\sigma} (x + iy) \phi_0(x, y) \right] \end{aligned} \quad (19)$$

where

$$\phi_0(x, y) = \left( \frac{1}{\pi\sigma^2} \right)^{\frac{1}{2}} e^{-\frac{x^2 + y^2}{2\sigma^2}}$$

This state is the two-dimensional Gaussian profile corresponding to the fundamental mode of the HG and LG states. As introduced in Sec. II, after the postselected measurement, the state of the pointer is changed to  $|\Psi\rangle$  (see Eq. (8)), and its expression in the coordinate representation is given by:

$$\begin{aligned} \Psi(x, y) &= \frac{\kappa}{\sqrt{1 + \gamma^2}} \{ t_- M_{-s} + t_+ M_{+s} + t_- T_- + t_+ T_+ \\ &\quad + t_- K_- + t_+ K_+ \} \end{aligned} \quad (20)$$

where  $t_\pm = 1 \pm \langle \sigma_x \rangle_x$ ,  $s = \Gamma/2$ ,  $M_{\pm s} = \phi_{\pm s}(x)\psi(y)$ ,  $K_\pm = i\frac{\sqrt{2}y}{\sigma}\gamma e^{i\varphi}\phi_{\pm s}(x)\psi(y)$ , and  $T_\pm =$



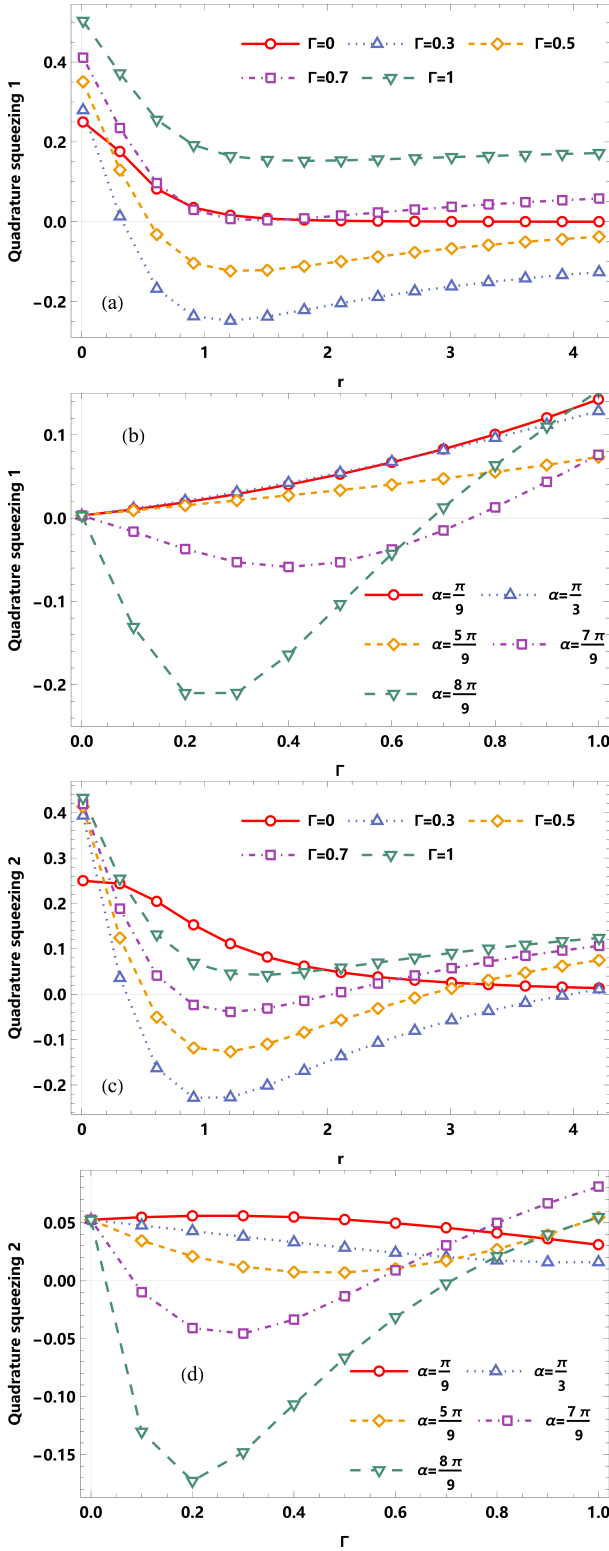


Figure 3. Quadratic squeezing parameters  $Q_1$  and  $Q_2$ . (a)  $Q_1$  as a function of  $r$  for different coupling strengths  $\Gamma$ , with the weak value fixed at  $\alpha = \frac{8\pi}{9}$ , (b)  $Q_1$  as a function of the weak value with coupling  $\Gamma$  at  $r = 2$ . (c)  $Q_2$  as a function of  $r$  for different coupling strengths  $\Gamma$ , with the weak value fixed at  $\alpha = \frac{8\pi}{9}$ . (d)  $Q_2$  as a function of the weak values characterized by  $\Gamma$  at  $r = 2$ . Here,  $\delta = 0$  and  $\varphi = \frac{\pi}{2}$ .

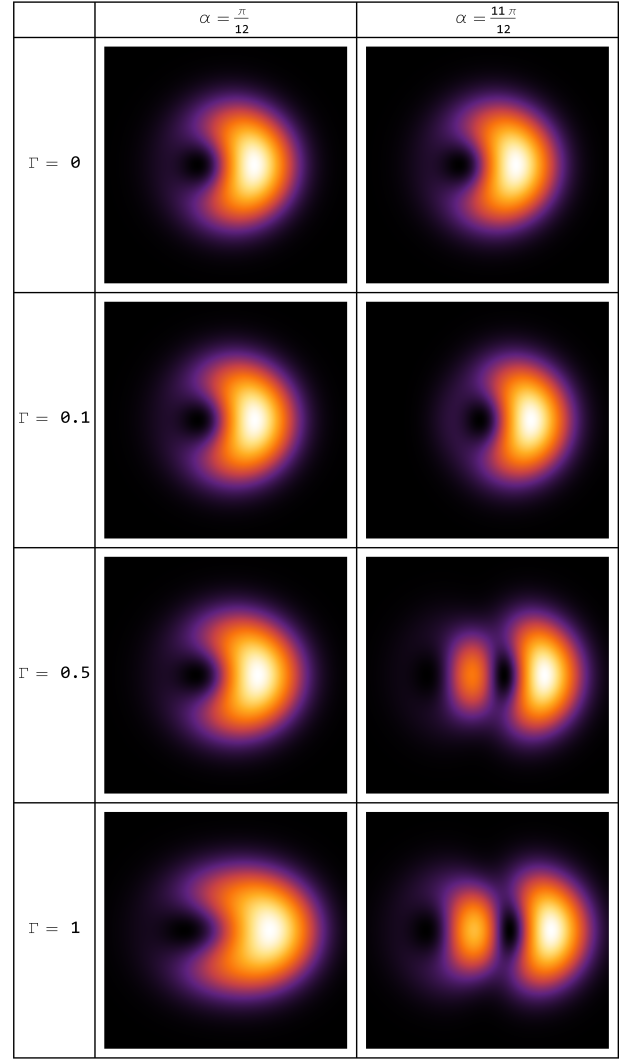


Figure 4. Intensity distribution after the postselected measurement for different measurement coupling strength parameter  $\Gamma$  and weak value parameter  $\alpha$ . Here we take  $\varphi = 0, \delta = 0, \sigma = 1$  and  $\gamma = 1$ .

$$\frac{\gamma e^{i\varphi}}{\sqrt{2}} \left[ \pm(1 - \sqrt{2})s + \frac{2x}{\sigma} \right] \phi_{\pm s}(x) \psi(y) \text{ with}$$

$$\phi_s(x) = \left( \frac{1}{\pi\sigma^2} \right)^{\frac{1}{4}} e^{-\frac{s^2}{2}} e^{\frac{x^2}{2\sigma^2}} e^{-\left(\frac{x}{\sigma} - \frac{s}{\sqrt{2}}\right)^2}, \quad (21)$$

and

$$\psi(y) = \left( \frac{1}{\pi\sigma^2} \right)^{\frac{1}{4}} e^{-\frac{y^2}{2\sigma^2}}. \quad (22)$$

To examine the effects of postselected von Neumann measurement on the spatial intensity profile of the superposition of LG modes defined in Eq. (1), we plot the intensity distribution of the state  $|\Psi\rangle$  as shown in Fig. 4. For comparison, in Fig. 4, we present the intensity distribution of the state  $|\Psi\rangle$  for small and large

weak values, as for different coupling strengths  $\Gamma$ . As indicated in the first column of Fig. 4, for small weak values, i.e.,  $\langle\sigma_x\rangle_w = 0.132$ , the spatial profile of  $|\Psi\rangle$  does not change dramatically and retains its initial shape as the coupling strength parameter  $\Gamma$  increases. As shown in the second column of Fig. 4, after a postselected measurement with a large weak value, i.e.,  $\langle\sigma_x\rangle_w = 7.596$ , the spatial intensity distribution of the initial state  $|\Psi_i\rangle$  changes significantly as  $\Gamma$  increases. In particular, for large weak values and  $\Gamma = 1$ , the intensity distribution of  $|\Psi\rangle$  separates into two parts, with each part exhibiting a zero-intensity region at the edges of the images, similar to the initial case. From the above analysis, we can confirm that the spatial intensity distribution of the OAM state notably changes when considering large weak values of the measured observable after a postselected von Neumann measurement. This intriguing result also suggests the potential applicability of postselected von Neumann measurements, characterized by weak values, in OAM-based state engineering processes.

## V. SECOND-ORDER CROSS-CORRELATION FUNCTION AND PHASE SPACE DISTRIBUTION

To further investigate the effects of postselected von Neumann measurement on the properties of  $|\Psi\rangle$ , in this section, we study the quantum statistics and phase space distribution of  $|\Psi\rangle$  for different system parameters.

### A. Second-order cross-correlation function

In this subsection, we study the second-order cross-correlation function  $g_{a,b}^{(2)}$  of  $|\Psi\rangle$ . The second-order cross-correlation function of a two-mode radiation field is defined as [66, 67]:

$$g_{a,b,\Psi}^{(2)} = \frac{\langle\hat{a}^\dagger\hat{a}\hat{b}^\dagger\hat{b}\rangle}{\langle\hat{a}^\dagger\hat{a}\rangle\langle\hat{b}^\dagger\hat{b}\rangle}, \quad (23)$$

here,  $\langle\hat{a}^\dagger\hat{a}\hat{b}^\dagger\hat{b}\rangle$  represents the intensity-intensity correlation between the two modes, and  $\langle\hat{a}^\dagger\hat{a}\rangle$  and  $\langle\hat{b}^\dagger\hat{b}\rangle$  denote the mean photon numbers for each mode, respectively. This correlation characterizes the relationship between photons in different modes. If  $g_{a,b,\Psi}^{(2)} > 1$ , there exists a correlation between the  $a$ -mode and  $b$ -mode of the two-mode radiation field; otherwise, the modes are inversely correlated. To analyze the properties of  $g_{a,b,\Psi}^{(2)}$ , we first derive the average values of  $\langle\hat{a}^\dagger\hat{a}\hat{b}^\dagger\hat{b}\rangle$ ,  $\langle\hat{a}^\dagger\hat{a}\rangle$ , and  $\langle\hat{b}^\dagger\hat{b}\rangle$  under the state  $|\Psi\rangle$ . Appendix A lists their explicit, cumbersome expressions.

To examine how the postselected von Neumann measurement affects the SOCC of the state  $|\Psi\rangle$ , we plot  $g_{a,b,\Psi}^{(2)}$  for different system parameters associated with the postselected von Neumann measurement. Fig. 5 presents the

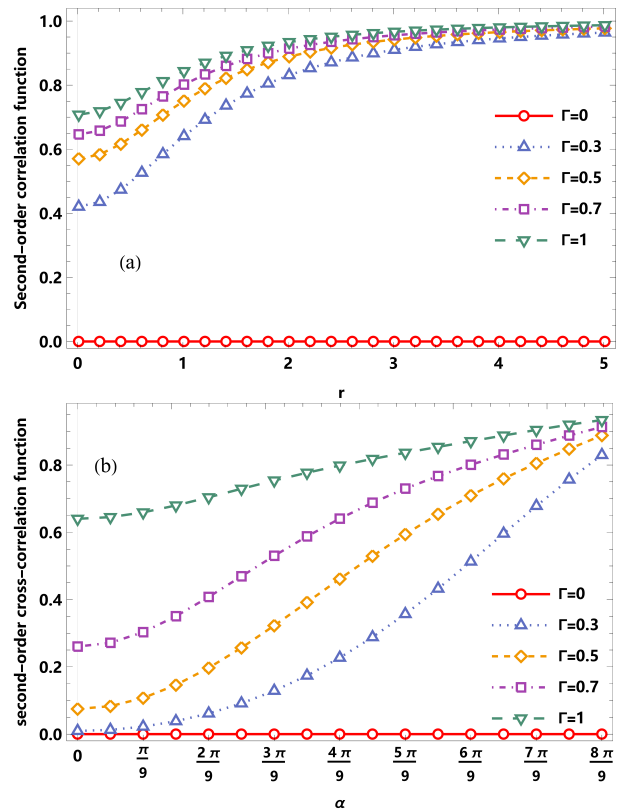


Figure 5. (a) Second-order cross-correlation as function of  $r$  for different coupling strengths  $\Gamma$ , with the weak value fixed at  $\alpha = \frac{8\pi}{9}$ . (b) Second-order cross-correlation as function of the weak value  $\alpha$  for different coupling strengths  $\Gamma$ , with  $r = 2$ . Here,  $\delta = 0$  and  $\varphi = \frac{\pi}{2}$ .

corresponding numerical results. The case  $\Gamma = 0$  corresponds to no interaction between the pointer and the measured system. Initially, we observe no correlation between the two modes of  $|\Psi\rangle$  (see the red-colored curves of Fig. 5). Our numerical results indicate that after the postselected measurement, no correlation occurs; however, as the weak value increases,  $g_{a,b,\Psi}^{(2)}$  approaches one. This behavior is due to the signal amplification effects of anomalously large weak values.

### B. Wigner function

To deeply understand the effects of postselected von Neumann measurements on the properties of  $|\Psi\rangle$ , we examine the phase space distribution by calculating its Wigner function. The general expression for the Wigner function of a state  $\rho = |\Psi\rangle\langle\Psi|$  is [68, 69]:

$$W(\alpha) \equiv \frac{1}{\pi^2} \int \int_{-\infty}^{+\infty} \exp(\beta^* \alpha - \beta \alpha^*) C_W(\beta) d^2\beta. \quad (24)$$

where  $C_W(\lambda)$  is the symmetrically ordered characteristic function, defined as:

$$C_W(\lambda) = \text{Tr} \left[ \rho e^{\lambda \hat{a}^\dagger - \lambda^* \hat{a}} \right]. \quad (25)$$

Here, we use the notation  $\lambda'$  and  $\lambda''$  for the real and imaginary parts of  $\lambda$ , and set  $\alpha = x + ip$  to emphasize the analogy between the quadratic radiation field and the normalized dimensionless position and momentum observables of the beam in phase space. We can rewrite the definition of the Wigner function in terms of  $x, p$  and  $\lambda', \lambda''$  as:

$$W(x, p) = \frac{1}{\pi^2} \int \int_{-\infty}^{+\infty} e^{2i(p\lambda' - x\lambda'')} C_W(\lambda) d\lambda' d\lambda''. \quad (26)$$

By substituting the final normalized pointer state  $|\Psi\rangle$  into Eq. (26), we obtain the explicit expression for  $W(x, p)$ . Due to its complexity, we have provided its full expression in the Appendix B. To illustrate the effects of the postselected von Neumann measurement on the non-classical features of  $|\Psi\rangle$  in phase space (SPACS), we plot the corresponding Wigner function in Fig. 6 for different values of  $r$  and the coupling strength  $\Gamma$ , with a fixed weak value of  $\langle \sigma_x \rangle_w = 5.671 (\alpha = \frac{8\pi}{9})$ .

Each column, from left to right, corresponds to different coupling strength parameters  $\Gamma = 0, 0.3, 0.5, 0.7, 1$ , while each row, from top to bottom, represents different values of  $r = 1, 2, 3, 4$ . The positive peak of the Wigner function shifts from the center to the edge of phase space, and its shape gradually becomes more irregular as  $\Gamma$  increases. From the first column (see Fig. 6), we can observe that the original state  $|\Psi'\rangle$  is a Gaussian state, and its Wigner function remains positive. In the second to fourth columns, corresponding to nonzero values of  $\Gamma$ , we see the phase space density function  $W(z)$  after the postselected von Neumann measurement. The distribution exhibits squeezing in phase space compared to the original state, and this squeezing becomes more pronounced as  $\Gamma$  increases.

Furthermore, Fig. 6 shows an increase in the negative regions of the Wigner function as  $\Gamma$  grows. The presence of larger negative regions indicates a greater degree of nonclassicality in the state. From this analysis, we conclude that after the postselected von Neumann measurement, the phase space distribution of  $|\Psi\rangle$  not only becomes squeezed but also exhibits enhanced nonclassicality for appropriate parameter values.

## VI. SIGNAL-TO-NOISE RATIO

In precision measurement, obtaining precise information while suppressing the associated noise is crucial. Previous studies [40] have investigated the advantages

of postselected von Neumann measurement using HG and LG modes as pointers. These studies claimed that higher-order modes of LG and HG beams do not offer any advantage in precision measurement compared to the zero-mean fundamental Gaussian beam, even with large anomalous weak values. The superposition of states can lead to interference phenomena and produce results that single states cannot. To evaluate the superiority of the state  $|\Psi\rangle$  over the fundamental Gaussian beam in post-selected precision measurement, we explore the SNR ratios between postselected and non-postselected measurements [69]:

$$\chi = \frac{\mathcal{R}_p}{\mathcal{R}_n}. \quad (27)$$

Here,  $\mathcal{R}_p$  represents the SNR of the postselected von Neumann measurement, which is defined by:

$$\mathcal{R}_p = \frac{\sqrt{NP_s} |\delta x|}{\Delta x} \quad (28)$$

with the variance of position operator

$$\Delta x = \sqrt{\langle \Psi | \hat{X}^2 | \Psi \rangle - \langle \Psi | \hat{X} | \Psi \rangle^2}, \quad (29)$$

and the average shift of the pointer variable  $x$  after post-selected measurement

$$\delta x = \langle \Psi | \hat{X} | \Psi \rangle - \langle \Psi_i | \hat{X} | \Psi_i \rangle. \quad (30)$$

Here,  $\hat{X} = \sigma (\hat{a} + \hat{a}^\dagger)$  is the position operator,  $N$  is the total number of measurements, and  $P_s$  is the probability of finding the postselected state for a given preselected state. For our scheme, this is given by  $P_s = |\langle \psi_f | \psi_i \rangle|^2 = \cos^2 \frac{\alpha}{2}$ , where  $NP_s$  represents the number of times the system is found in the postselected state  $|\psi_f\rangle$ . By using the expressions for the states  $|\Psi_i\rangle$  and  $|\Psi\rangle$  given in Eq. (4) and Eq. (8), we can obtain:

$$\langle \Psi_i | \hat{X} | \Psi_i \rangle = 2\sigma \Re [\langle \Psi_i | \hat{a} | \Psi_i \rangle], \quad (31)$$

$$\langle \Psi | \hat{X} | \Psi \rangle = 2\sigma \Re [\langle \Psi | \hat{a} | \Psi \rangle], \quad (32)$$

$$\langle \Psi | \hat{X}^2 | \Psi \rangle = \sigma^2 \{ 2\langle \Psi | \hat{a}^\dagger \hat{a} | \Psi \rangle + 2\Re [\langle \Psi | \hat{a}^2 | \Psi \rangle] + 1 \},$$

Furthermore, when dealing with non-postselected measurements, there is no postselection process after the interaction between the system and the pointer. Thus, the definition of SNR  $\mathcal{R}_n$  for non-postselected weak measurement can be given as:

$$\mathcal{R}_n = \frac{\sqrt{N} |\delta x'|}{\Delta x'}. \quad (33)$$

with

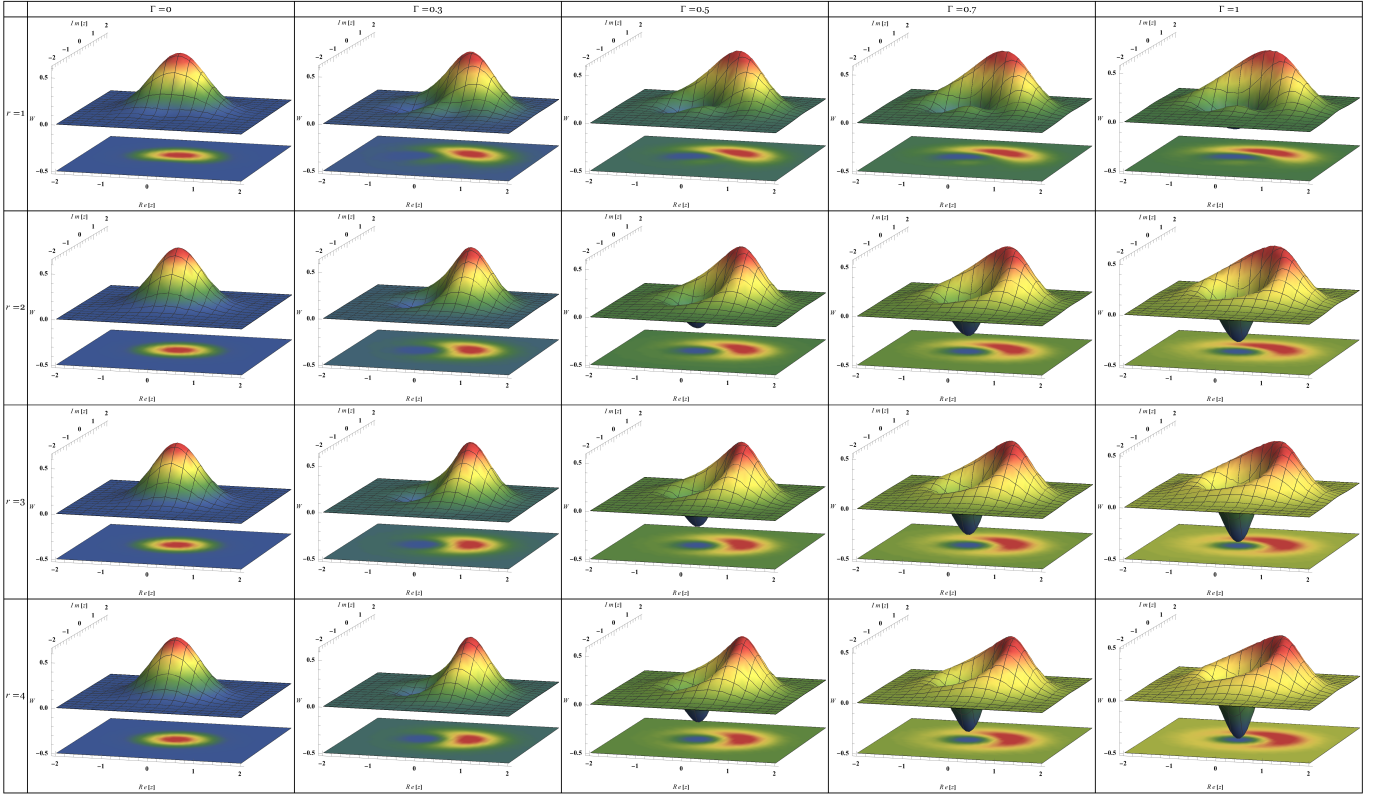


Figure 6. Wigner function of  $|\Psi\rangle$  for different system parameters. Here, we set  $\varphi = 0$ ,  $\delta = 0$ , and  $\alpha = \frac{8\pi}{9}$ .

$$\Delta x' = \sqrt{\langle \Phi | \hat{X}^2 | \Phi \rangle - \langle \Phi | \hat{X} | \Phi \rangle^2}, \quad (34)$$

$$\delta x' = \langle \Phi | \hat{X} | \Phi \rangle - \langle \Psi_i | \hat{X} | \Psi_i \rangle. \quad (35)$$

Here,  $\langle \Phi | \hat{X} | \Phi \rangle$  denotes the expectation value of the measuring observable under the final state of the pointer without postselection, which can be derived from Eq. (7). To evaluate the ratio  $\chi$  of SNRs, we need to calculate the related quantities, and the corresponding expressions are given as:

$$\langle \Psi_i | \hat{X}_1 | \Psi_i \rangle = 2\sigma \Re[\langle \Psi_i | \hat{a} | \Psi_i \rangle], \quad (36)$$

$$\langle \Phi | \hat{X}_1 | \Phi \rangle = 2\sigma \Re[\langle \Phi | \hat{a} | \Phi \rangle], \quad (37)$$

$$\langle \Phi | \hat{X}_1^2 | \Phi \rangle = \sigma^2 \{ 2\langle \Phi | \hat{a}^\dagger \hat{a} | \Phi \rangle + 2\Re[\langle \Phi | \hat{a}^2 | \Phi \rangle] + 1 \} \quad (38)$$

where the expectation values of  $\langle \hat{a} \rangle$ ,  $\langle \hat{a}^\dagger \hat{a} \rangle$  and  $\langle \hat{a}^2 \rangle$  under the state  $|\Phi\rangle$  are given as

$$\langle \hat{a} \rangle = \frac{\gamma e^{i\varphi}}{\sqrt{2}(1+\gamma^2)} + \frac{\Gamma}{2} \sin \alpha \cos \delta, \quad (39)$$

$$\langle \hat{a}^\dagger \hat{a} \rangle = \frac{\gamma^2}{2(1+\gamma^2)} + \frac{\Gamma^2}{4}, \quad (40)$$

$$\langle \hat{a}^2 \rangle = \frac{\Gamma^2}{4} + \frac{\Gamma \gamma e^{i\varphi} (1 + \sin \alpha \cos \delta)}{\sqrt{2}(1+\gamma^2)}, \quad (41)$$

The ratio of SNRs between postselected and non-postselected weak measurement is plotted as a function of the coupling strength parameter  $\Gamma$  and  $r$ , respectively, with the results shown in Figs. 3(a) and 3(b). As observed in Fig. 3(a), the ratio  $\chi$  increases and can become greater than unity with increasing weak values in the weak measurement regime. In Fig. 3(b), we plot the ratio  $\chi$  as a function of  $r$  for different weak values while fixing the coupling parameter at  $\Gamma = 0.2$ . The numerical results indicate that, in our scheme, anomalous weak values are indeed helpful for increasing the SNR in weak measurement regimes. From this result, we can deduce that postselected measurements improve the precision of measurement compared to the non-postselected case. Additionally, our superposition state  $|\Psi_i\rangle$  can be used in the postselected von Neumann process considering large weak values of the measured observable.

## VII. CONCLUSION AND OUTLOOKS

As investigated in Ref. [70], postselected measurements have demonstrated advantages in quantum metrology and are particularly useful in precision measurement processes. In this work, our results based on the superposition of LG pointer states further confirm the effectiveness of postselected measurements in state optimization and precision measurements. We explored the effects of



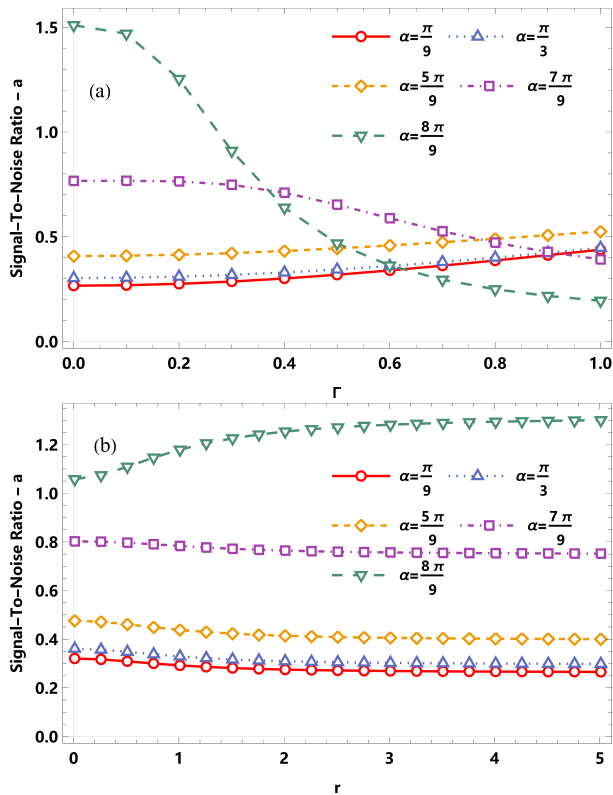


Figure 7. (a) The ratio  $\chi$  as a function of the coupling strength  $\Gamma$  for different weak values, with  $r = 2$ . (b) The ratio  $\chi$  as a function of  $r$  for different weak values, with the coupling strength at  $\Gamma = 0.2$ . Here, we set  $\delta = 0$  and  $\varphi = \frac{\pi}{2}$ .

postselected von Neumann measurements on the properties of superpositions of Gaussian and Laguerre-Gaussian states. Throughout the work, we avoided approximations, providing precise analytical results for all related quantities. First, we presented analytical and numerical results for the quadrature squeezing of the final pointer state. Our findings indicate that quadrature squeezing increased significantly in the weak measurement regime for anomalous weak values. By analyzing the second-order cross-correlation function, we found no quantum correlation between the two modes of the state  $|\Psi_i\rangle$ , even when signal amplification via large anomalous weak values was employed. We also investigated the phase space distribution of the final pointer state  $|\Psi\rangle$ . While the initial state  $|\Psi_i\rangle$  is a typical Gaussian state, its Gaussianity changed after applying postselected measurements. Specifically, the negativity of the Wigner function for the superpositions of Gaussian and Laguerre-Gaussian states

increased with the coupling strength parameter and weak values. In the phase space distribution, squeezing in two quadratures was also observed after the postselected measurement. These results demonstrate that postselected von Neumann measurements can transform the state  $|\Psi_i\rangle$  from a classical state to a nonclassical one by selecting appropriate coupling strength parameters and weak values of the measured system's observables. Furthermore, comparing the signal-to-noise ratio between postselected and non-postselected measurement schemes shows that the SNR in the postselected measurement scheme is significantly higher than in the non-postselected scheme within the weak measurement regime, particularly for large weak values. Despite the low probability of successful postselection, the amplification effect of weak values plays a crucial role throughout this work. This study contributes to the domain of state optimization using postselected measurements. However, the most widely used quantum state engineering method in quantum optics remains the addition or subtraction of single photons to/from a light field [71]. This approach to state optimization and manipulation can be applied to single and multimode quantum states of light [72, 73]. Beyond photon addition and subtraction, or their superpositions, quantum catalysis is also a feasible method for generating nonclassical quantum states [74]. Compared to these existing state optimization techniques, the postselected von Neumann measurement-based method offers a universal approach applicable to diverse quantum states. A von Neumann-type interaction Hamiltonian can always be constructed by selecting two independent degrees of freedom from the associated states. Consequently, it would be interesting to investigate the effects of postselected von Neumann measurements on other Gaussian and non-Gaussian multipartite continuous-variable radiation fields [75–77], including two-photon coherent states [78–80], three-mode states [81, 82] and other multimode radiation fields [83].

## ACKNOWLEDGMENTS

This work is supported by the National Natural Science Foundation of China (Grants No. 12365005 and No. 11865017).

## Appendix A: Relevant expressions

The expectation values of some relevant operators under the state  $|\Psi\rangle$  are listed below:

$$\langle \hat{a} \rangle = \frac{|\lambda|^2}{2} \left\{ (1 + |\langle \sigma_x \rangle_w|^2) \frac{\gamma e^{i\varphi}}{\sqrt{2}(1 + \gamma^2)} + (1 - |\langle \hat{\sigma}_x \rangle_w|^2) II + (1 - I_2) \Gamma \Re[\langle \sigma_x \rangle_w] \right\}, \quad (\text{A1})$$

$$\langle \hat{b} \rangle = \frac{|\lambda'|^2 i \sqrt{2} \gamma e^{i\varphi}}{4(1+\gamma^2)} \left[ 1 + |\langle \sigma_x \rangle_w|^2 + (1 - |\langle \sigma_x \rangle_w|^2) e^{-\frac{\Gamma^2}{2}} \right] + \frac{|\lambda'|^2 \gamma^2 \Gamma}{4(1+\gamma^2)} (\langle \sigma_x \rangle_w^* - \langle \sigma_x \rangle_w) e^{-\frac{\Gamma^2}{2}}, \quad (\text{A2})$$

$$\begin{aligned} \langle \hat{a}^2 \rangle &= \frac{|\lambda'|^2 \Gamma}{2} \left[ \left( \frac{\sqrt{2} \gamma e^{i\varphi}}{1+\gamma^2} + 2II \right) \Re[\langle \sigma_x \rangle_w] + (1 + |\langle \sigma_x \rangle_w|^2) \frac{\Gamma}{4} \right] \\ &+ \frac{|\lambda'|^2 \Gamma^2}{16} [(1 + \langle \sigma_x \rangle_w^*) (1 - \langle \sigma_x \rangle_w) I_2 + (1 - \langle \sigma_x \rangle_w^*) (1 + \langle \sigma_x \rangle_w) I_1], \end{aligned} \quad (\text{A3})$$

$$\langle \hat{b}^2 \rangle = 0, \quad (\text{A4})$$

$$\begin{aligned} \langle \hat{a}^\dagger \hat{a} \rangle &= \frac{|\lambda'|^2}{2} (1 + |\langle \sigma_x \rangle_w|^2) \left( \frac{\gamma^2}{2(1+\gamma^2)} + \frac{\Gamma^2}{4} \right) + i \frac{|\lambda'|^2 \Gamma \gamma \cos(\varphi)}{2\sqrt{2}(1+\gamma^2)} \Im[\langle \sigma_x \rangle_w] + \frac{|\lambda'|^2}{4} (1 + \langle \sigma_x \rangle_w^*) (1 - \langle \sigma_x \rangle_w) III_+ \\ &+ \frac{|\lambda'|^2}{4} (1 - \langle \sigma_x \rangle_w^*) (1 + \langle \sigma_x \rangle_w) III_- + \frac{|\lambda'|^2 \Gamma^2}{16} [(1 + \langle \sigma_x \rangle_w^*) (1 - \langle \sigma_x \rangle_w) I_2 + (1 - \langle \sigma_x \rangle_w^*) (1 + \langle \sigma_x \rangle_w) I_1] \\ &+ \frac{|\lambda'|^2 \Gamma}{8} [(1 - \langle \sigma_x \rangle_w^*) (1 + \langle \sigma_x \rangle_w) (IV_1 + II_1) - (1 + \langle \sigma_x \rangle_w^*) (1 - \langle \sigma_x \rangle_w) (IV_2 + II_2)], \end{aligned} \quad (\text{A5})$$

$$\langle \hat{b}^\dagger \hat{b} \rangle = \frac{|\lambda'|^2}{4} \left[ (1 + |\langle \sigma_x \rangle_w|^2) \frac{\gamma^2}{1+\gamma^2} + (1 - |\langle \sigma_x \rangle_w|^2) \frac{\gamma^2}{1+\gamma^2} e^{-\frac{\Gamma^2}{2}} \right], \quad (\text{A6})$$

$$\begin{aligned} \langle \hat{a}^\dagger \hat{b} \rangle &= \frac{|\lambda'|^2}{4} \left[ (1 + |\langle \sigma_x \rangle_w|^2) \frac{i\gamma^2}{(1+\gamma^2)} + (\langle \sigma_x \rangle_w - \langle \sigma_x \rangle_w^*) \frac{i\Gamma\gamma e^{i\varphi}}{\sqrt{2}(1+\gamma^2)} \left( 1 + e^{-\frac{\Gamma^2}{2}} \right) + (1 - |\langle \sigma_x \rangle_w|^2) \frac{\gamma^2}{2(1+\gamma^2)} \Gamma^2 e^{-\frac{\Gamma^2}{2}} \right] \\ &+ \frac{|\lambda'|^2}{4} [(1 + \langle \sigma_x \rangle_w^*) (1 - \langle \sigma_x \rangle_w) B_+ + (1 - \langle \sigma_x \rangle_w^*) (1 + \langle \sigma_x \rangle_w) B_-], \end{aligned} \quad (\text{A7})$$

$$\langle \hat{a} \hat{b} \rangle = \frac{|\lambda'|^2}{4} \left[ ((\langle \sigma_x \rangle_w + \langle \sigma_x \rangle_w^*) + (\langle \sigma_x \rangle_w - \langle \sigma_x \rangle_w^*) e^{-\frac{\Gamma^2}{2}}) \frac{\Gamma i \gamma e^{i\varphi}}{\sqrt{2}(1+\gamma^2)} + \frac{|\lambda'|^2}{4} (1 - |\langle \sigma_x \rangle_w|^2) \frac{\gamma^2}{2(1+\gamma^2)} \Gamma^2 e^{-\frac{\Gamma^2}{2}} \right], \quad (\text{A8})$$

$$\langle \hat{a}^\dagger \hat{a} \hat{b}^\dagger \hat{b} \rangle = \frac{|\lambda'|^2}{4} \frac{\Gamma^2 \gamma^2}{4(1+\gamma^2)} \left[ 1 + |\langle \sigma_x \rangle_w|^2 - (1 - |\langle \sigma_x \rangle_w|^2) e^{-\frac{\Gamma^2}{2}} \right], \quad (\text{A9})$$

$$\begin{aligned} \langle \hat{a}^{\dagger 2} \hat{a}^2 \rangle &= \frac{|\lambda'|^2}{4} [(1 - \langle \sigma_x \rangle_w^*) (1 - \langle \sigma_x \rangle_w) M_- + (1 + \langle \sigma_x \rangle_w^*) (1 + \langle \sigma_x \rangle_w) M_+] \\ &+ \frac{|\lambda'|^2}{4} [(1 - \langle \sigma_x \rangle_w^*) (1 + \langle \sigma_x \rangle_w) M_3 + (1 + \langle \sigma_x \rangle_w^*) (1 - \langle \sigma_x \rangle_w) M_4], \end{aligned} \quad (\text{A10})$$

$$\langle \hat{b}^{\dagger 2} \hat{b}^2 \rangle = 0, \quad (\text{A11})$$

with

$$I_2 = \frac{e^{-\frac{\Gamma^2}{2}}}{1+\gamma^2} \left[ 1 + \gamma^2 + \sqrt{2} \Gamma \gamma i \sin(\varphi) - \frac{\gamma^2 \Gamma^2}{2} \right], \quad (\text{A12})$$

$$II = \frac{\gamma e^{i\varphi} e^{-\frac{\Gamma^2}{2}}}{\sqrt{2}(1+\gamma^2)}, \quad (\text{A13})$$

$$III_{\pm} = \frac{e^{-\frac{\Gamma^2}{2}}}{1 + \gamma^2} \left[ \frac{\gamma^2}{2} (1 - \Gamma^2) \pm \frac{\gamma e^{i\varphi}}{\sqrt{2}} \Gamma \right], \quad (\text{A14})$$

$$B_{\pm} = \frac{\pm i \gamma e^{-\frac{\Gamma^2}{2}}}{1 + \gamma^2} \left[ \frac{\gamma}{2} (1 - \Gamma^2) - \frac{e^{\pm i\varphi}}{\sqrt{2}} \Gamma \right], \quad (\text{A15})$$

$$M_{\pm} = \frac{\Gamma^2 \gamma^2}{2(1 + \gamma^2)} \pm \frac{\Gamma^3 \gamma \cos(\varphi)}{2\sqrt{2}(1 + \gamma^2)} + \frac{\Gamma^4}{16}, \quad (\text{A16})$$

$$M_3 = \Gamma T_{11} + \frac{\Gamma^2}{4} (T_{21} + 4IV_1) + \frac{\Gamma^3}{4} (V_1 + II_1) + \frac{\Gamma^4 I_1}{16}, \quad (\text{A17})$$

$$M_4 = \frac{\Gamma^2}{4} (T_{22} + 4IV_2) - \Gamma T_{12} - \frac{\Gamma^3}{4} (V_2 + II_2) + \frac{\Gamma^4 I_2}{16}, \quad (\text{A18})$$

$$T_{11} = \frac{\gamma e^{i\varphi} \Gamma}{1 + \gamma^2} \left[ \frac{\Gamma}{\sqrt{2}} - \gamma e^{-i\varphi} \left(1 - \frac{\Gamma^2}{2}\right) \right] e^{-\frac{\Gamma^2}{2}}, \quad (\text{A19})$$

$$T_{21} = \frac{\Gamma^2}{1 + \gamma^2} \left[ 1 + \gamma^2 \left(2 - \frac{\Gamma^2}{2}\right) \right] e^{-\frac{\Gamma^2}{2}}, \quad (\text{A20})$$

$$IV_1 = \frac{e^{-\frac{\Gamma^2}{2}}}{1 + \gamma^2} \left[ \frac{\gamma^2}{2} (1 - \Gamma^2) - \frac{\gamma e^{i\varphi}}{\sqrt{2}} \Gamma \right], \quad (\text{A21})$$

$$IV_2 = \frac{e^{-\frac{\Gamma^2}{2}}}{1 + \gamma^2} \left[ \frac{\gamma^2}{2} (1 - \Gamma^2) + \frac{\gamma e^{i\varphi}}{\sqrt{2}} \Gamma \right], \quad (\text{A22})$$

$$V_1 = \frac{e^{-\frac{\Gamma^2}{2}}}{2(1 + \gamma^2)} \left[ \Gamma^2 \gamma e^{i\varphi} + \sqrt{2} \gamma e^{-i\varphi} (1 - \Gamma^2) - 2\Gamma - \Gamma \gamma^2 \left(1 + \frac{2 - \Gamma^2}{\sqrt{2}}\right) \right], \quad (\text{A23})$$

$$V_2 = \frac{e^{-\frac{\Gamma^2}{2}}}{2(1 + \gamma^2)} \left[ \Gamma^2 \gamma e^{i\varphi} + \sqrt{2} \gamma e^{-i\varphi} (1 - \Gamma^2) + 2\Gamma + \Gamma \gamma^2 \left(1 + \frac{2 - \Gamma^2}{\sqrt{2}}\right) \right], \quad (\text{A24})$$

$$T_{12} = \frac{\gamma e^{i\varphi} \Gamma}{1 + \gamma^2} \left[ \frac{\Gamma}{\sqrt{2}} + \gamma e^{-i\varphi} \left(1 - \frac{\Gamma^2}{2}\right) \right] e^{-\frac{\Gamma^2}{2}}, \quad (\text{A25})$$

$$T_{22} = \frac{\Gamma^2}{1 + \gamma^2} \left[ 1 + \gamma^2 \left(2 - \frac{\Gamma^2}{2}\right) \right] e^{-\frac{\Gamma^2}{2}}, \quad (\text{A26})$$

### Appendix B: Wigner function

The explicit expression of the Wigner function of our final pointer state  $|\Psi\rangle$  can be calculated as following:

$$W(\alpha) = \frac{|\lambda|^2}{4} \{ |1 - \langle \sigma_x \rangle_w|^2 W_+ + |1 + \langle \sigma_x \rangle_w|^2 W_- + 2\Re[(1 + \langle \sigma_x \rangle_w^*) (1 - \langle \sigma_x \rangle_w) W_1] \}, \quad (\text{B1})$$

where

$$W_{\pm} = \frac{1}{\pi} \left\{ 2 + \frac{2\gamma\sqrt{2}}{1+\gamma^2} [(2x \pm \Gamma) \cos(\varphi) + 2b \sin(\varphi)] + \frac{\gamma^2}{1+\gamma^2} [4p^2 + (2x \pm \Gamma)^2 - 2] \right\} e^{-2p^2 - \frac{(2x \pm \Gamma)^2}{2}}, \quad (\text{B2})$$

$$W_1 = \frac{e^{-\frac{\Gamma^2}{2}}}{\pi} \left\{ 2 + \frac{4\gamma\sqrt{2}}{1+\gamma^2} [x \cos(\varphi) + p \sinh(\varphi)] + \frac{2\gamma^2}{(1+\gamma^2)} (2x^2 + 2p^2 - 1) \right\} e^{-2x^2 - \frac{(2p - i\Gamma)^2}{2}}, \quad (\text{B3})$$

- 
- [1] J. F. Nye and M. V. Berry, *Proc.R.Soc.London.Ser.A* **336**, 165 (1974).
- [2] V. I. Bazhenov, M. Vasnetsov, and M. Soskin, *JETP Lett.* **52**, 1037 (1990).
- [3] H. Kobayashi, K. Nonaka, and M. Kitano, *Opt. Express* **20**, 14064 (2012).
- [4] A. White, C. Smith, N. Heckenberg, H. Rubinsztein-Dunlop, R. McDuff, C. Weiss, and C. Tamm, *J Mod Opt* **38**, 2531 (1991).
- [5] N. R. Heckenberg, R. McDuff, C. P. Smith, and A. G. White, *Opt. Lett.* **17**, 221 (1992).
- [6] L. Allen, M. W. Beijersbergen, R. J. C. Spreeuw, and J. P. Woerdman, *Phys. Rev. A* **45**, 8185 (1992).
- [7] M. Beijersbergen, R. Coerwinkel, M. Kristensen, and J. Woerdman, *Opt. Commun* **112**, 321 (1994).
- [8] L. Marrucci, C. Manzo, and D. Paparo, *Phys. Rev. Lett.* **96**, 163905 (2006).
- [9] T. Ando, Y. Ohtake, N. Matsumoto, T. Inoue, and N. Fukuchi, *Opt. Lett.* **34**, 34 (2009).
- [10] M. Mansuripur, A. R. Zakharian, and E. M. Wright, *Phys. Rev. A* **84**, 033813 (2011).
- [11] J. Kim and W. A. Clarkson, *Opt. Commun* **296**, 109 (2013).
- [12] B. Xia, J. Huang, H. Li, M. Liu, T. Xiao, C. Fang, and G. Zeng, *Photonics Res* (2022).
- [13] R. Horodecki, P. Horodecki, M. Horodecki, and K. Horodecki, *Rev. Mod. Phys.* **81**, 865 (2009).
- [14] V. Vedral, *NAT PHYS* **10**, 256 (2014).
- [15] J. Tavares, *Revista de Ciência Elementar* (2023).
- [16] L. Allen, M. W. Beijersbergen, R. J. C. Spreeuw, and J. P. Woerdman, *Phys. Rev. A* **45**, 8185 (1992).
- [17] D. G. Grier, *nature* **424**, 810 (2003).
- [18] G. Gibson, J. Courtial, M. J. Padgett, M. Vasnetsov, V. Pas'ko, S. M. Barnett, and S. Franke-Arnold, *Opt. Express* **12**, 5448 (2004).
- [19] J. Wang, J.-Y. Yang, I. M. Fazal, N. Ahmed, Y. Yan, H. Huang, Y. Ren, Y. Yue, S. Dolinar, M. Tur, *et al.*, *Nat.Photon* **6**, 488 (2012).
- [20] N. Bozinovic, Y. Yue, Y. Ren, M. Tur, P. Kristensen, H. Huang, A. E. Willner, and S. Ramachandran, *Science* **340**, 1545 (2013).
- [21] M. Krenn, J. Handsteiner, M. Fink, R. Fickler, R. Ursin, M. Malik, and A. Zeilinger, *Proc. Natl. Acad. Sci.* **113**, 13648 (2016).
- [22] M. P. J. Lavery, C. Peuntinger, K. Günthner, P. Banzer, D. Elser, R. W. Boyd, M. J. Padgett, C. Marquardt, and G. Leuchs, *Sci Adv* **3**, e1700552 (2017).
- [23] S. Groblacher, T. Jennewein, A. Vaziri, G. Weihs, and A. Zeilinger, *New J. Phys* **8**, 75 (2006).
- [24] A. Sit, F. Bouchard, R. Fickler, J. Gagnon-Bischoff, H. Larocque, K. Heshami, D. Elser, C. Peuntinger, K. Günthner, B. Heim, C. Marquardt, G. Leuchs, R. W. Boyd, and E. Karimi, *Optica* **4**, 1006 (2017).
- [25] A. Nicolas, L. Veissier, L. Giner, E. Giacobino, D. Maxein, and J. Laurat, *Nat.Photon* **8**, 234 (2014).
- [26] R. Juchtmans, A. Béch e, A. Abakumov, M. Batuk, and J. Verbeeck, *Phys. Rev. B* **91**, 094112 (2015).
- [27] B. Jack, J. Leach, J. Romero, S. Franke-Arnold, M. Ritsch-Marte, S. M. Barnett, and M. J. Padgett, *Phys. Rev. Lett.* **103**, 083602 (2009).
- [28] S. F urhapter, A. Jesacher, S. Bernet, and M. Ritsch-Marte, *Opt. Express* **13**, 689 (2005).
- [29] P. Prentice, M. Macdonald, T. Frank, A. Cuschieri, G. C. Spalding, W. Sibbett, P. Campbell, and K. Dholakia, *Optics express* **12** **4**, 593 (2004).
- [30] Y. Aharonov, D. Z. Albert, and L. Vaidman, *Phys. Rev. Lett.* **60**, 1351 (1988).
- [31] Y. Turek, *Communications in Theoretical Physics* **72**, 055504 (2020).
- [32] Y. Turek, *Eur. Phys. J. Plus* **136**, 221 (2021), [arXiv:2006.08081 \[quant-ph\]](https://arxiv.org/abs/2006.08081).
- [33] W. J. Xu, T. Yusufu, and Y. Turek, *Phys. Rev. A* **105**, 022210 (2022).
- [34] Q. Hu, T. Yusufu, and Y. Turek, *Phys. Rev. A* **105**, 022608 (2022).
- [35] Y. Turek, J. Yuanbek, and A. Abliz, *Physics Letters A* **462**, 128663 (2023).
- [36] Y. Turek, A. Islam, and A. Abliz, *Eur. Phys. J. Plus* **138**, 72 (2023), [arXiv:2109.10128 \[quant-ph\]](https://arxiv.org/abs/2109.10128).
- [37] Y. Turek, N. Aishan, and A. Islam, *Phys. Scripta* **98**, 075103 (2023), [arXiv:2212.10222 \[quant-ph\]](https://arxiv.org/abs/2212.10222).
- [38] Y. Turek, *CHINESE PHYS B* **29**, 090302 (2020).
- [39] M. R. Dennis and J. B. G tte, *New J. Phys* **14**, 073013 (2012).
- [40] Y. Turek, H. Kobayashi, T. Akutsu, C.-P. Sun, and Y. Shikano, *New J. Phys* **17**, 083029 (2015).
- [41] H. Kobayashi, K. Nonaka, and Y. Shikano, *Phys. Rev. A* **89**, 053816 (2014).
- [42] J. Qiu, C. Ren, and Z. Zhang, *Phys. Rev. A* **93**, 063841 (2016).
- [43] J. Zhu, P. Zhang, Q. Li, F. Wang, C. Wang, Y. Zhou, J. Wang, H. Gao, L. C. Kwek, and F. Li, *Scientific Reports* **9**, 7993 (2019).
- [44] J. B. G tte and M. R. Dennis, *New J. Phys* **14**, 073016 (2012).
- [45] M. R. Dennis and J. B. G tte, *Phys. Rev. Lett.* **109**,



- 183903 (2012).
- [46] J. B. Götte and M. R. Dennis, *Opt. Lett.* **38**, 2295 (2013).
- [47] O. S. Magaña Loaiza, M. Mirhosseini, B. Rodenburg, and R. W. Boyd, *Phys. Rev. Lett.* **112**, 200401 (2014).
- [48] J. Leach, M. J. Padgett, S. M. Barnett, S. Franke-Arnold, and J. Courtial, *Phys. Rev. Lett.* **88**, 257901 (2002).
- [49] A. Belmonte and J. P. Torres, *Opt. Lett.* **37**, 2940 (2012).
- [50] G. C. G. Berkhout, M. P. J. Lavery, J. Courtial, M. W. Beijersbergen, and M. J. Padgett, *Phys. Rev. Lett.* **105**, 153601 (2010).
- [51] P. Genevet, J. Lin, M. A. Kats, and F. Capasso, *Nat. Commun* **3**, 1278 (2012).
- [52] K. Saitoh, Y. Hasegawa, K. Hirakawa, N. Tanaka, and M. Uchida, *Phys. Rev. Lett.* **111**, 074801 (2013).
- [53] G. Guzzinati, L. Clark, A. Béch e, and J. Verbeeck, *Phys. Rev. A* **89**, 025803 (2014).
- [54] L. Clark, A. B ech e, G. Guzzinati, and J. Verbeeck, *Phys. Rev. A* **89**, 053818 (2014).
- [55] A. Vaziri, G. Weihs, and A. Zeilinger, *J. opt* **4**, S47 (2002).
- [56] A. Mair, A. Vaziri, G. Weihs, and A. Zeilinger, *Nature* (2001), 10.1038/35085529.
- [57] B. Jack, A. M. Yao, J. Leach, J. Romero, S. Franke-Arnold, D. G. Ireland, S. M. Barnett, and M. J. Padgett, *Phys. Rev. A* **81**, 043844 (2010).
- [58] F. Yue, D. Wen, C. Zhang, B. D. Gerardot, W. Wang, S. Zhang, and X. Chen, *Advanced Materials* **29**, 1603838 (2017), <https://onlinelibrary.wiley.com/doi/pdf/10.1002/adma.201607688>.
- [59] V. V. Kotlyar, A. A. Kovalev, and A. P. Porfirev, *Opt. Express* **27**, 11236 (2019).
- [60] B. P. da Silva, B. A. D. Marques, R. B. Rodrigues, P. H. S. Ribeiro, and A. Z. Houry, *Phys. Rev. A* **103**, 063704 (2021).
- [61] X. Wu, Z. Wang, and B. Yu, *J. Opt. Soc. Am. B* **41**, 768 (2024).
- [62] B. de Lima Bernardo, S. Azevedo, and A. Rosas, *Opt. Commun* **331**, 194 (2014).
- [63] J. von Neumann, *Mathematical Foundations of Quantum Mechanics*, edited by N. A. Wheeler (Princeton University Press, Princeton, 2018).
- [64] Y. Pan, J. Zhang, E. Cohen, C.-w. Wu, P.-X. Chen, and N. Davidson, *Nat. Phys* **16**, 1206 (2020).
- [65] G. Adesso, S. Ragy, and A. R. Lee, *Open Syst. Inf. Dyn.* **21** (2014).
- [66] G. Ren, W. hai Zhang, and Y. jun Xu, *Physica A* **520**, 106 (2019).
- [67] S. K. Giri, K. Thapliyal, B. Sen, and A. Pathak, *Physica A* **466**, 140 (2017).
- [68] C. Gerry and P. Knight, *Introductory Quantum Optics* (Cambridge University Press, Cambridge, England, 2004).
- [69] G. Agarwal, *Quantum Optics* (Cambridge University Press, Cambridge, England, 2013).
- [70] D. R. M. Arvidsson-Shukur, N. Yunger Halpern, H. V. Lepage, A. A. Lasek, C. H. W. Barnes, and S. Lloyd, *Nat. Commun.* **11**, 3775 (2020).
- [71] V. Parigi, A. Zavatta, M. Kim, and M. Bellini, *Science* **317**, 1890 (2007).
- [72] V. Averchenko, C. Jacquard, V. Thiel, C. Fabre, and N. Treps, *New J. Phys.* **18**, 083042 (2016).
- [73] H. Tomoda, A. Machinaga, K. Takase, J. Harada, T. Kashiwazaki, T. Umeki, S. Miki, F. China, M. Yabuno, H. Terai, D. Okuno, and S. Takeda, *Phys. Rev. A* **110**, 033717 (2024).
- [74] A. I. Lvovsky and J. Mlynek, *Phys. Rev. Lett.* **88**, 250401 (2002).
- [75] A. I. Lvovsky, P. Grangier, A. Ourjoumtsev, V. Parigi, M. Sasaki, and R. Tualle-Brouri, (2020), [arXiv:2006.16985 \[quant-ph\]](https://arxiv.org/abs/2006.16985).
- [76] M. Walschaers, *PRX Quantum* **2**, 030204 (2021).
- [77] W. Asavanant and A. Furusawa, *Phys. Rev. A* **109**, 040101 (2024).
- [78] G. S. Agarwal, *J. Opt. Soc. Am. B* **5**, 1940 (1988).
- [79] Z. Z. Xin, D. B. Wang, M. Hirayama, and K. Matumoto, *Phys. Rev. A* **50**, 2865 (1994).
- [80] H. P. Yuen, *Phys. Rev. A* **13**, 2226 (1976).
- [81] D. M. Greenberger, M. A. Horne, A. Shimony, and A. Zeilinger, *Am. J. Phys.* **58**, 1131 (1990).
- [82] G. Giedke, B. Kraus, M. Lewenstein, and J. I. Cirac, *Phys. Rev. A* **64**, 052303 (2001).
- [83] K. J. Blow, R. Loudon, S. J. D. Phoenix, and T. J. Shepherd, *Phys. Rev. A* **42**, 4102 (1990).